Volume 6 | Number 25 | 7 July 2018 | Pages 4167–4266

Journal of Materials Chemistry B

Materials for biology and medicine

rsc.li/materials-b

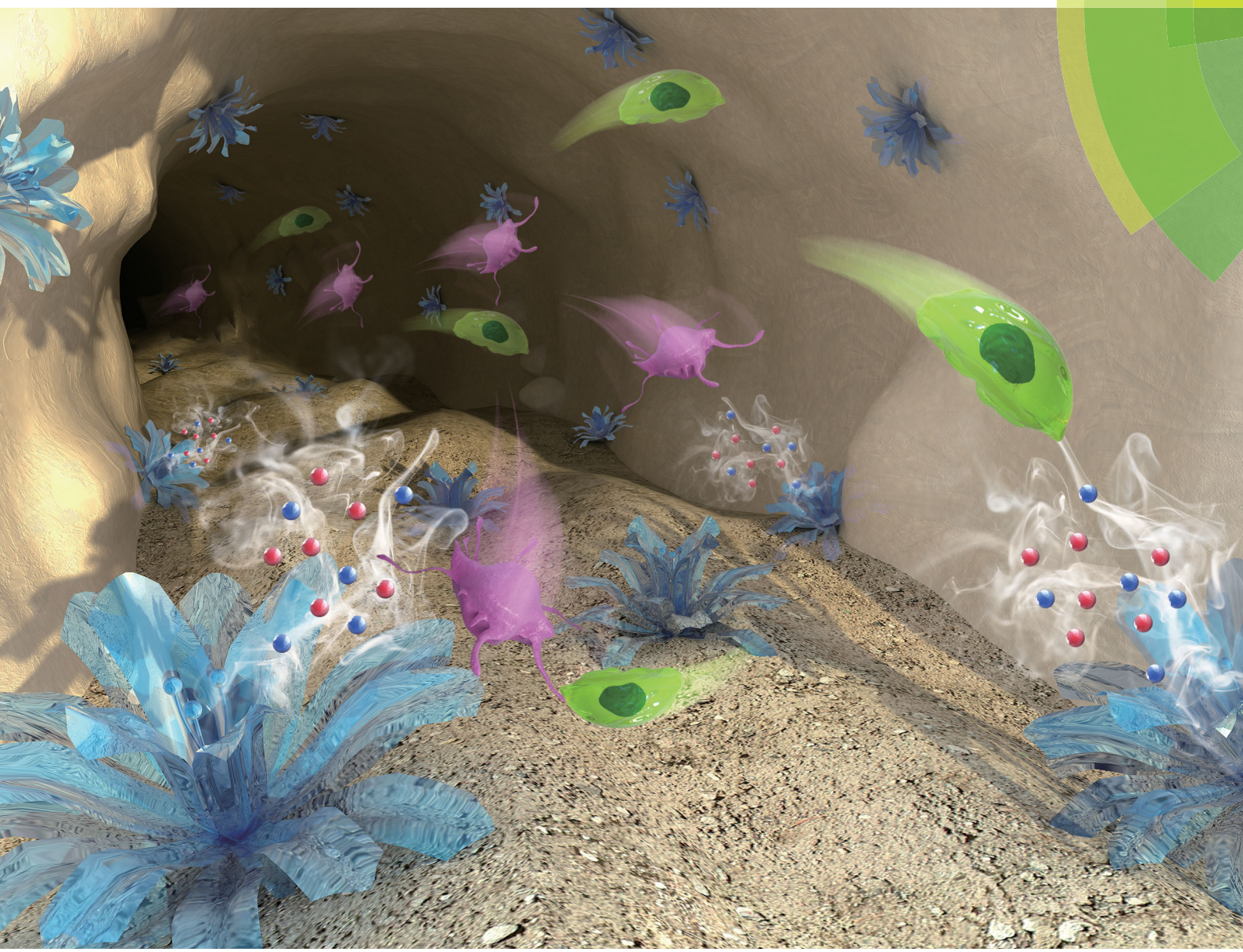

ISSN 2050-750X

ROYAL SOCIETY OF CHEMISTRY

PAPER

Xi-Le Hu, Yaping Li, Tingting Tang *et al.*

Osteogenesis, vascularization and osseointegration of a bioactive multiphase macroporous scaffold in the treatment of large bone defects

Journal of Materials Chemistry B

PAPER

View Article Online
View Journal | View Issue

Cite this: J. Mater. Chem. B, 2018, 6, 4197

Osteogenesis, vascularization and osseointegration of a bioactive multiphase macroporous scaffold in the treatment of large bone defects

Linyang Chu,[a] Guoqiang Jiang,[b] Xi-Le Hu,*[c] Tony D. James,[d] Xiao-Peng He,[c] Yaping Li*[b] and Tingting Tang*[a]

Received 20th March 2018,
Accepted 7th May 2018

DOI: 10.1039/c8tb00766g

rsc.li/materials-b

Bone grafting remains the method of choice for the majority of surgeons in the treatment of large bone defects, since it fills spaces and provides support to enhance biological bone repair. Recently, we have reported our research on a bioactive multiphase macroporous scaffold with interconnected porous structures and nano-crystal surface microstructures that can release bioactive ions. Moreover, we demonstrated the excellent *in vitro* biological activity of the scaffold. In this study, we set out to evaluate the *in vivo* osteogenesis and vascularization of the scaffold in the treatment of large bone defects (10 mm radial bone defect in rabbits). In comparison with the control group, X-ray and micro-CT results at the 4th and 8th week post-surgery reveal that the bioactive scaffold displayed an enhanced level of new bone and vessel formation. Histological results at the same weeks indicated improved bone formation, osseointegration and new vessel ingrowth inside the bioactive scaffold. These findings establish a good foundation for the potential clinical validation of the bioactive macroporous biomaterial scaffold for use as a bone substitute or in tissue engineering.

1. Introduction

Autologous bones are the gold standard of graft materials, providing many active factors for bone ingrowth. However, problems still exist, such as resorption, fatigue failure, fracture, secondary infection and the limited supply of autologous bones.[1–3] Therefore, research on the development of bone substitute materials for potential clinical validation is an important focus of medical research.[4] Biomaterial scaffolds have been developed extensively for bone restoration.[5–7] However, an ideal bone substitute or a tissue engineering scaffold should be osteoinductive, osteoconductive, and biocompatible and possess an interconnected structure with high porosity.[8] Hydroxyapatite (HA, $Ca_5(PO_4)_3(OH)$) has been considered to be a good substitute for bone tissue regeneration due to its recognized compatibility and osteoconductivity. However, its brittleness, low mechanical stability and high stability in the human body limit its application in bone tissue engineering.[8,9] Additionally, previous studies have suggested that single-phase materials could not perfectly meet the needs of tissue engineering scaffolds.[10,11]

To overcome these problems, multiphase materials modified and functionalized by various chemical processes in order to render them bioactive are urgently required. It has been reported that the osteogenic capacity and mechanical properties of biomaterials could be improved by chemical modification, *i.e.*, by the formation of functional sulfo groups or chemical–mechanical polishing.[12,13] Chemical modification for bone substitutes or scaffolds could lead to diversified bioactivity as well as new opportunities for bone tissue engineering (Scheme 1).

In our previous investigation, we used hydrothermal calcination to develop bioactive multiphase macroporous scaffolds with interconnected porous, nano-crystal surface microstructures capable of releasing bioactive ions.[14] We demonstrated that these bioactive scaffolds with good biocompatibility possessed excellent osteogenesis and vascularization capacity *in vitro*. Moreover, we determined that the scaffold exhibited excellent efficacy for tissue integration in a dorsum subcutaneous implantation model. These results unambiguously provided a basis for subsequent *in vivo* investigations. Therefore, in the present study, we sought to examine the potential of the scaffold for bone regeneration using a standard segmental radial bone defect model in rabbits.

[a] Shanghai Key Laboratory of Orthopedic Implants, Department of Orthopedic Surgery, Shanghai Ninth People's Hospital, Shanghai Jiao Tong University School of Medicine, Shanghai 200011, P. R. China. E-mail: ttt@sjtu.edu.cn
[b] Department of Orthopaedic Surgery, Affiliated Hospital of School of Medicine, Ningbo University, Ningbo 315211, P. R. China. E-mail: liyaping36@126.com
[c] Key Laboratory for Advanced Materials and Joint International Research Laboratory of Precision Chemistry and Molecular Engineering, Feringa Nobel Prize Scientist Joint Research Center, School of Chemistry and Molecular Engineering, East China University of Science and Technology, 130 Meilong Rd., Shanghai 200237, China. E-mail: xlhu@ecust.edu.cn
[d] Department of Chemistry, University of Bath, Bath, BA2 7AY, UK

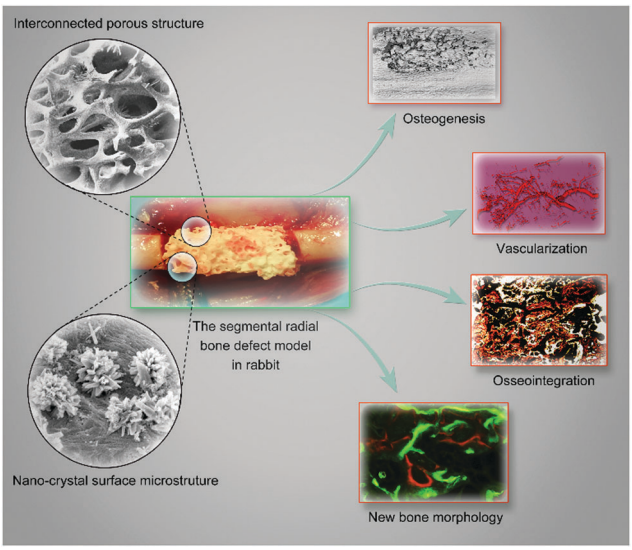

Scheme 1 A segmental radial bone defect model used to evaluate the *in vivo* osteogenesis, vascularization and osseointegration of the bioactive multiphase macroporous scaffold with interconnected porous, nano-crystal surface microstructures that can release bioactive ions.

Techniques including radiographs, micro-CT and histological analyses were used. Since it is known that bioactive material scaffolds can promote neovascularization in order to further facilitate the osteogenic potential,[15] the present study also adopted angiography to test vessel formation within the scaffold and local blood perfusion. We envision that the bioactive macroporous scaffold could be an ideal biomaterial for use as a bone substitute or in tissue engineering.

2. Experimental section

2.1 Materials

The bioactive macroporous scaffold was fabricated according to our previous method.[14] In brief, the calcined and cleaned bovine cancellous bone (its main composition is HA) and a solution of Mg^{2+}, PO_4^{3-} and SO_4^{2-} were mixed, and the system was then subjected to the hydrothermal reaction for 36 h at 75 °C. The scaffold was then placed in a temperature-controlled calcination furnace at 1050 °C for 6 h to obtain the desired HA/Ca/Mg scaffold (additional $Ca_{(3-n)}Mg_n(PO_4)_2$ and $CaSO_4$ were produced). The HA/Ca/Mg scaffold preserved the natural interconnected porous structure, connectivity and pore size. Nano-crystal, whisker-like microstructures were formed on the HA/Ca/Mg scaffold surface. A pure HA scaffold without hydrothermal reaction and a macroporous scaffold (TCP) widely used in clinical practice were used as controls.[16,17]

2.2 Characterization of scaffolds used *in vivo*

All scaffolds used in an animal model were trimmed into cylinders with a diameter of 4 mm and a length of 10 mm in order to fit into bone defects. The scaffolds were dried, coated by gold sputtering, and examined using a scanning electron microscope (SEM, Japan) at an electron acceleration voltage of 1.5 kV in the secondary electron detection mode to visualize the surface microstructure.

2.3 Establishment of segmental radial bone defects in rabbits

A segmental radial bone defect model in adult male rabbits was used in the present study.[18–21] All procedures were approved and performed in accordance with the guidelines of the Animal Ethics Committee of Shanghai Ninth People's Hospital. In brief, male rabbits of 5 months old weighing 3.5–4 kg were anaesthetized with ear intravenous injection of 1.5% pentobarbital (1 mL kg^{-1}). Then, bilateral forelimbs of rabbits were shaved, prepped with 70% ethanol, and then the radius was exposed through a longitudinal incision of the skin. A segment of the radial bone with a length of 10 mm, which was regarded as a sub-critical sized defect, was surgically removed. Scaffolds were press fit into the radial defects and the wound was carefully closed with layers of sutures. Pressure bandages were used to protect the wound for three post-surgery days.

2.4 X-ray evaluation of newly formed bones

High-resolution radiographs of the operated radius were taken at post-operative weeks of 0, 4 and 8, using an X-ray machine (Faxitron X-ray Corporation, USA) with an exposure time of 3 s.[22]

2.5 Micro-CT evaluation of newly formed bones

At post-operative weeks 4 and 8, newly formed bones were characterized using a high-resolution micro-CT (Scanco Medical, μCT-80, Switzerland) at an isometric resolution of 10 μm according to published protocols.[19] Briefly, the bony compartment was segmented from the marrow and soft tissue for subsequent analyses using a global threshold procedure. A threshold equal to or above 150 represented bony tissue; a threshold below 150 represented bone marrow, soft tissue and implanted composite scaffolds.[23] The new bone formed within the bone defect region was acquired for the quantification of tissue volume (TV), bone volume (BV) and bone mineral density (BMD).

2.6 Micro-CT evaluation of vascularization

Microfil perfusion was conducted in the forelimbs of rabbits. Briefly, under deep general anaesthesia, the bilateral *arteria axillaris* and *vena axillaris* of the animals were separated and needles were inserted that were linked to a pump apparatus with a flow speed at 20 mL min^{-1} for perfusion. The vasculature was adequately flushed with pre-warmed heparinized saline and injected with a solution of Microfil (Microfil, Flow Tech, Inc., USA) prepared in a volume ratio of 4/5 of Microfil/diluent with 5% curing agent based on the manufacturer's protocol.[18] Then, bilateral forelimbs were harvested, fixed with 4% neutral-buffered formaldehyde for 48 h and decalcified with 9% formic acid for 4 weeks. The vascularization of radial defects was reconstructed using micro-CT at an isometric resolution of 10 μm. The three-dimensional reconstruction of the newly formed vessels and their volume were analyzed by the software provided by the manufacturer.[24] The evaluation was obtained using four samples randomly selected from each group.

2.7 Decalcified histological evaluation

The samples were fixed in 10% neutral-buffered formaldehyde for 3 days, decalcified for 1 week using Rapidly Decalcifier (DeCa DX-1000; Pro-Cure Medical Technology Co Ltd, Hong Kong) and then embedded in paraffin. Finally, the sections of specimens at a thickness of 5 μm were prepared along the long axis and the coronal plane of the radial defect region using a microtome (CUT 6062; SLEE Medical, Germany).

The sections with H&E, Giemsa, Safranin O-fast green, Sirius red and Masson's trichrome staining were digitalized into a microscopic system for the descriptive histology of the appearance of newly formed bones and quantitative histomorphometry.[18,25–27] The area of newly formed bones in the total implant area within the bone defects was quantified separately using an Image-Pro Plus software system (Media Cybernetics, USA).[19] Four serial sections from each sample were used to provide an average for statistical analysis. Meanwhile, CD31 immunohistochemistry was used to assess vessel ingrowth. The sections were dewaxed in alcohol, rehydrated and immersed into 3% hydrogen peroxide to block endogenous peroxidases and then rinsed in PBS. The slides were immersed into 0.1% Triton-X100 to allow penetration of the membrane for 15 min. Antigen retrieval was carried out in a 10 mM warm citrate buffer for 15 min. Specific sites were saturated with normal goat serum for 40 min at 37 °C. The monoclonal anti-CD31 antibody (ab76533, Abcam) was used. The sections were incubated with biotinylated rabbit anti-rabbit immunoglobulins, washed in TBS for 5 min and incubated for 30 min with streptavidin–peroxidase (1 : 50, DAKO). The nuclei were counter-stained with H&E for 2–3 s, washed in distilled water and finally covered with Aquatex (Merck, Germany).

2.8 Undecalcified histological evaluation

Two fluorescence dyes, calcein and alizarin red, were used to test the bone dynamic remodeling within segmental bone defects using established protocols.[28] In brief, calcein (10 mg kg^{-1}) and alizarin red (30 mg kg^{-1}) were injected subcutaneously and sequentially into the rabbits of weeks 4 and 8 at day 14 and day 7 before euthanasia. The samples of the radial bone defects were fixed in 10% neutral-buffered formaldehyde for 2 days. Then, the samples were placed into an embedded device containing the methylmethacrylate (MMA, Merck-Schuchardt, Germany) monomer and stored at 4 °C. After 1 week, the MMA monomer was discarded. Colloidal MMA was added and stored at room temperature until being solidified. The embedded fragments containing the tissue specimens were collected and cut into 150 μm sections using a microtome (SP1600, Leica, Germany). Then, the sections were adhered to organic glass slides and compressed for 24 h. The thickness of the section was polished to 50 μm using P600, P800, and P1200 abrasive paper followed by burnishing with flannelette and abradum to 20–30 μm.

The fluorescence of the new bones formed was visualized by confocal laser scanning microscopy (CLSM, Leica, Germany). Then at least four sections of each implant were stained with picric acid/fuchsin.[28] Briefly, the histological sections were soaked in 1% formic acid for 3 min, rinsed with running water for 5 min, and dried. Then the histological sections were soaked in 20% methanol for 2 h, and then picric acid/fuchsin staining was performed. The histological sections were preheated at 60 °C, stained with Stevenol's blue for 5–15 min, rinsed with distilled water and dried, stained with the VG staining solution for 3–8 min, cleaned with pure ethanol, and dried. An optical microscope (Leica Microsystems AG, Germany) was used for histological evaluation. Finally, the area of newly formed bones was calculated using Image-Pro Plus software. Four sections were examined microscopically for statistical analysis.

2.9 Statistical analysis

All data are expressed as mean ± SD. Nonparametric test (Mann–Whitney U test), one-way analysis of variance (ANOVA) and the least significant difference (LSD) test were utilized to determine the level of significance; $p < 0.05$ was defined as statistically significant, and $p < 0.01$ was considered highly statistically significant. All statistical analyses of the data were performed using SPSS software (v19.0, USA).

3. Results and discussion

3.1 Establishment of segmental radial bone defects and characterization of scaffolds used *in vivo*

Despite rapid advances, osteogenesis and vascularization of large bone grafts remain a major challenge hampering the clinical translation of bone substitutes or tissue engineering scaffolds.[1,7,29] The transformation of animal bone materials with ideal three-dimensional interconnected porous structures has attracted significant attention in recent years.[10,11] The ability of bone substitute materials to provide both accelerated osteogenesis and vascularization is regarded as the gold standard. In our previous work,[14] we demonstrated excellent biocompatibility, osteogenesis and vascularization of a HA/Ca/Mg scaffold possessing nano-crystal surface microstructures capable of releasing bioactive ions *in vitro*. These positive *in vitro* results laid a solid foundation for subsequent *in vivo* research. In this study, we established a segmental radial bone defect model in rabbits (Fig. 1B). The scaffolds used in the animal model with a diameter of 4 mm and a length of 10 mm are shown in Fig. 1A. The surface morphologies of HA and HA/Ca/Mg scaffolds were characterized using SEM. The micrograph showed that the HA/Ca/Mg scaffold had a nano-crystal whisker microstructure, which was consistent with our previous observations.[14] Moreover, we used a macroporous scaffold (TCP), which has been widely used in clinical practice,[16,17] as control for the *in vivo* bioactivity of the HA/Ca/Mg scaffold.

3.2 X-ray and micro-CT evaluation of newly formed bones

A bioactive scaffold should have the ability to stimulate a biological response in order to achieve effective osteogenesis at the position of the bone defect. For successful osteogenesis, the scaffold should exhibit highly bioactive interactions with osteoblasts.[30–32] The regenerative ability of the scaffold could

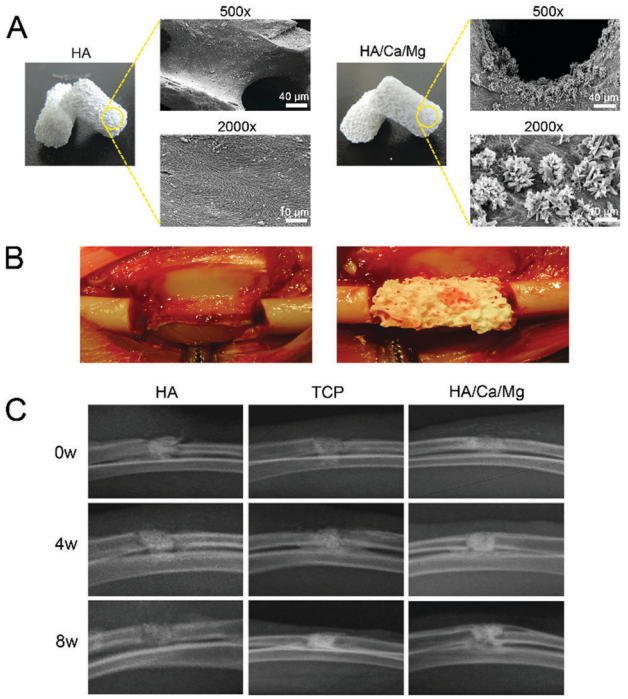

Fig. 1 (A) Scaffolds used in the animal model and SEM images of the surface morphology of the scaffolds. (B) Scaffold with a diameter of 4 mm and a length of 10 mm was implanted into the segmental rabbit radial bone defect. (C) Radiographs of radial segmental defects with different implants taken at weeks 0, 4 and 8.

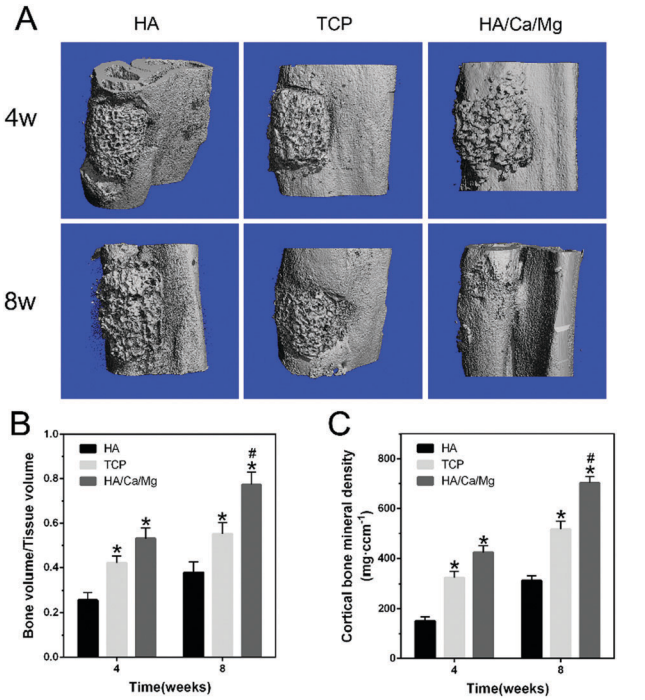

Fig. 2 (A) Representative micro-CT images of segmental radial defects reconstructed at weeks 4 and 8. (B and C) Bone volume and BMD within the defects of the radius evaluated at weeks 4 and 8. *$p < 0.05$ compared with HA scaffolds. $^{\#}p < 0.05$ compared with TCP scaffolds.

be improved by optimizing the biomaterial composition and properties or by the incorporation of bioactive ions that play a pivotal role in tissue repair.[33] In our previous study,[14] we demonstrated that the presence of a nano-crystal surface microstructure on bioactive scaffolds could effectively enhance cell attachment, spreading, proliferation and formation of focal adhesions, thus improving the cytocompatibility of the scaffold *in vitro*. Meanwhile, the bioactive Ca^{2+} and Mg^{2+} ions released from the HA/Ca/Mg scaffold exerted a positive influence on the osteogenic differentiation of pre-osteoblasts. In this study, the *in vivo* radial bone defect healing was analyzed by X-ray and micro-CT to assess the osteogenic potential of the HA/Ca/Mg scaffold. The results of X-ray analysis shown in Fig. 1C suggest that the different scaffolds used had varied degrees of bone healing efficacy. The best cortical regeneration and continuous bone callus formation were found in the HA/Ca/Mg group at weeks 4 and 8. We observed newly formed bones around and inside the HA/Ca/Mg scaffolds, effectively repairing the radial bone defects. The healing effect of the TCP scaffold was better than that of the HA scaffold alone at weeks 4 and 8, and the HA scaffold displayed the slowest healing rate. The results of micro-CT (Fig. 2A) again indicated that the bone formation in the HA group was relatively smooth at week 4. However, different portions of bone contacts were observed around TCP and HA/Ca/Mg scaffolds. At week 8, the efficiency of new bone formation in the defects of the HA/Ca/Mg group was remarkably higher than those of the other groups. The volume of new bones (BV/TV) and BMD within the bone defects at weeks 4 and 8 were calculated and are given in Fig. 2B and C, from which it is clear that the HA/Ca/Mg scaffold contained the highest bone volume and BMD ($P < 0.05$).

3.3 Micro-CT evaluation of vascularization

Vascularization at an early stage after implantation is known to provide necessary oxygen and nourishment for cell repair, tissue ingrowth and bone reconstruction.[19,34] Importantly, it has been demonstrated that vascularization could establish a microvascular system providing blood throughout the entire scaffold, which supports osteogenesis in bone defects.[35,36] Moreover, vascularization for tissue regeneration can precede osteogenesis by well-established mechanisms, and the enhanced neovascularization can accelerate new bone formation.[37,38] In the present study, the formation of new blood vessels in the radial bone defects at weeks 4 and 8 was analyzed using the Microfil experiment. The 3D images of neovascularization within the bone defect regions are given in Fig. 3A. After 4 and 8 weeks of implantation, abundant vessels were vividly displayed inside the HA/Ca/Mg scaffold, whereas fewer blood vessels were seen inside the HA and TCP scaffolds. Compared with the HA and TCP groups, the HA/Ca/Mg group presented more new vessels with respect to the total vessel volume growing into the defects at weeks 4 and 8 ($p < 0.05$, Fig. 3B). The vessel number within the scaffolds at weeks 4 and 8 post-implantation is given in Fig. 3C. The HA/Ca/Mg group showed more newly formed vessels with perfused microfil located within the scaffolds at weeks 4 and 8,

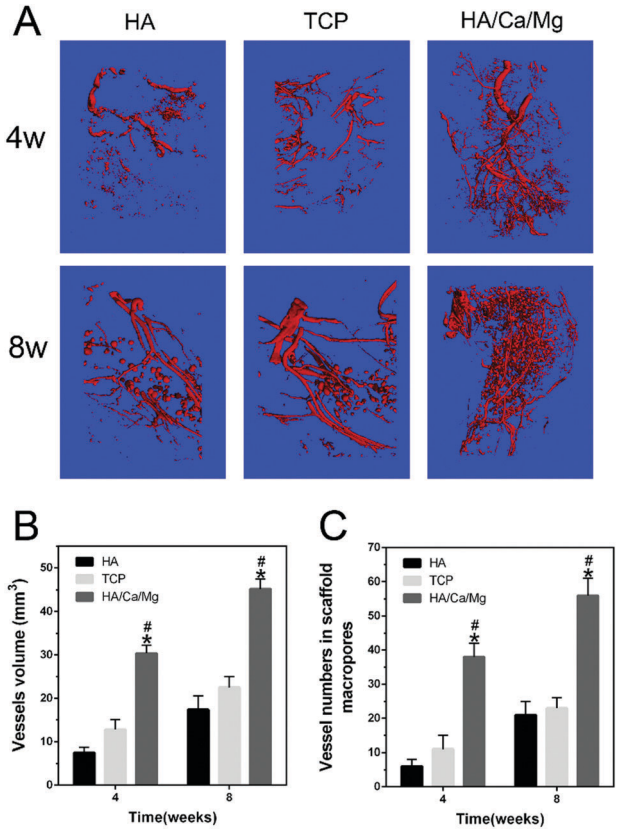

Fig. 3 (A) Representative micro-CT based angiography of vessels formed within the radial segmental defect region at weeks 4 and 8. (B and C) Vessel volume and vessel numbers within the defects evaluated at weeks 4 and 8. *$p < 0.05$ compared with HA scaffolds. #$p < 0.05$ compared with TCP scaffolds.

with a significant difference between HA and TCP groups ($p < 0.05$). These results were consistent with the *in vitro* study that the bioactive scaffold could promote the vascularization process.[14] According to the *in vivo* test, we hypothesized that the excellent ability of osteogenesis was partly due to its outstanding vascularization ability. It has been reported that the vascularization process *in vivo* is influenced by many factors, such as porosity, local active ion release and secretion of growth factors.[39–41]

3.4 Decalcified histological evaluation

Biomaterials with a homogeneous, interconnected porous structure are required for bone substitutes or tissue engineering.[42,43] An ideal porosity is conducive to cell recruitment of bone repair, vascular access, oxygen and tissue fluid exchange, and provides a good physiologically active space for bone ingrowth.[15] In our previous study, we demonstrated that the HA/Ca/Mg scaffold possessed relatively appropriate pore size, porosity and high pore connectivity.[14] Histological observations were performed to analyse in more detail the regeneration process for the different scaffolds. The H&E and Giemsa staining results of the radial bone defects implanted with scaffolds for 4 and 8 weeks are shown in Fig. 4A and C. After implantation for 4 weeks, we observed that the HA scaffold pores were filled with loose fibrous connective tissue, and osteogenesis was barely detected. While in the TCP and HA/Ca/Mg groups, some newly formed bony bridging was seen in the defect region, which grew gradually into the central zone and the macropores of the scaffolds, closely combining with trabeculae of the scaffolds. We determined that more bone matrix was deposited directly inside the pores in the HA/Ca/Mg scaffold than that in the TCP group, suggesting a good osseointegration inside the former scaffold. At week 8, the largest mature lamellar bone tissue was formed in the HA/Ca/Mg group, suggesting the best osteoconductivity and biocompatibility of the scaffold. Meanwhile, as shown in Fig. 4B and D, we also used Safranin O-fast green and Sirius red staining to reveal extensive collagenous matrix formation with the different scaffolds. After implantation for 4 and 8 weeks, we determined that bone defect healing was mostly marked by soft tissue callus formation in the HA scaffold. In the HA/Ca/Mg scaffold, we observed an intricate, dense and strong staining collagen matrix arrangement, which suggested that type I collagen, the main component of bone, was the largest component. Masson's trichrome staining was used to assess the changes in the bone morphology as shown in Fig. 5A; the results indicated that the new bones originated from bone defect edges gradually formed along the external margins of the implant towards the centre of the scaffolds. The quantitative staining results of the new bone area are shown in Fig. 5B, where it was revealed that, at week 4, the newly formed bone in TCP and HA/Ca/Mg groups were greater than that of the HA group ($p < 0.05$), but there was no significant difference between the two groups ($p > 0.05$). However, at week 8, the HA/Ca/Mg group showed the largest new bone growth for all the scaffolds evaluated ($p < 0.01$). These results indicate that the bones could grow or migrate into the scaffolds through the macropores of the scaffolds, and denser bone regeneration was found in the HA/Ca/Mg scaffold compared to the other scaffolds, which allowed a higher osteogenesis efficiency *in vivo*. Furthermore, the results of CD31 immunohistochemistry indicated a much better vascularization of the HA/Ca/Mg scaffold than the other scaffolds (Fig. 5C), which was in agreement with the results obtained by micro-CT.

3.5 Undecalcified histological evaluation

The osseointegration efficiency, which represents the direct contact between the newly formed bone and the implant, also reflects the biocompatibility and other functions of the implant interface; therefore, an integrated bone–implant interface could facilitate long-term sustained osteogenesis.[28,44,45] We used fluorescence labelling and undecalcified histological analysis to evaluate the osseointegration inside implants at the defects of the radius. The morphological changes in osteointegration between newly formed bones and implant trabeculae on the transverse sections stained with Van Gieson are shown in Fig. 6A.

At week 4, the minimal bone contact was observed around the HA scaffold, but obviously new bone tissues were in close contact with trabeculae on the edge of the TCP and HA/Ca/Mg scaffolds. At week 8, the bone tissue grown inside the HA scaffolds was also limited, while the HA/Ca/Mg scaffolds were

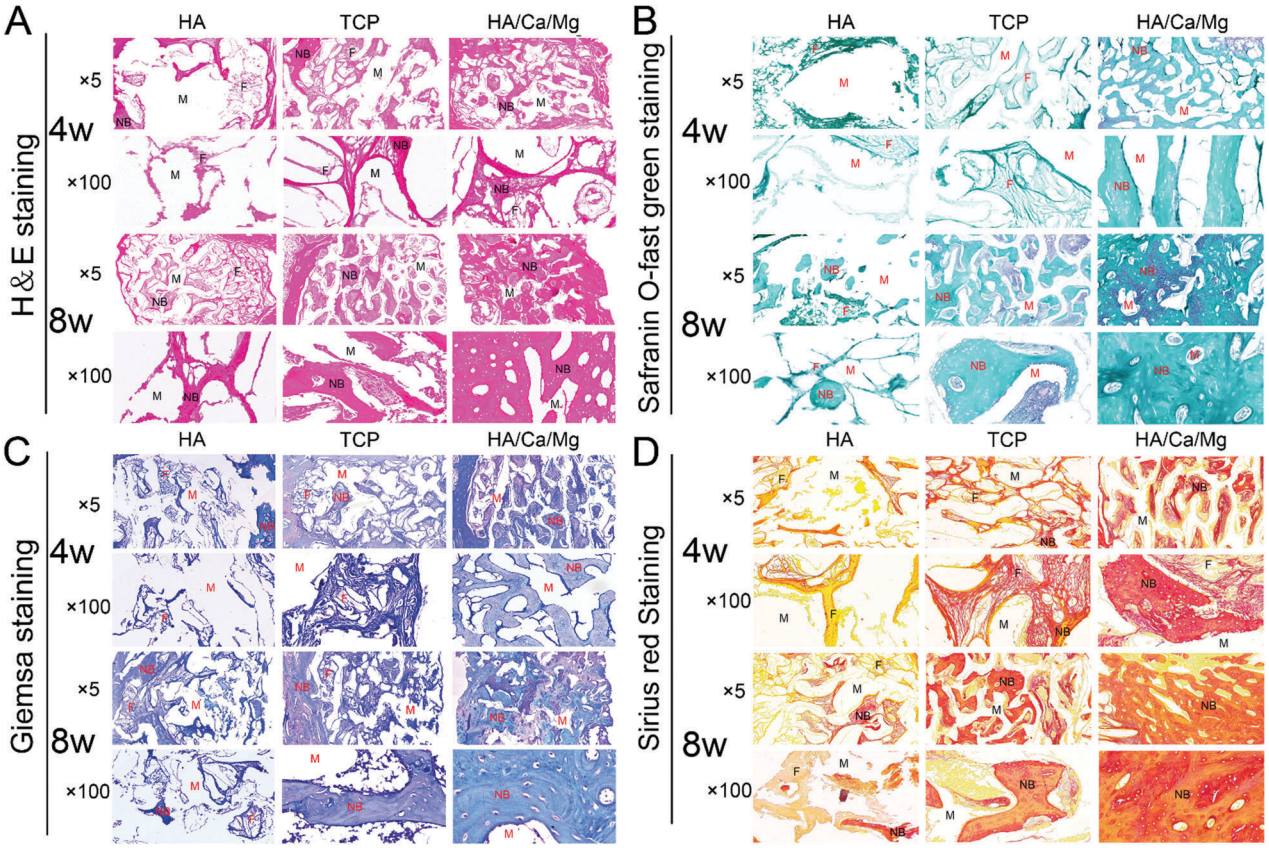

Fig. 4 Representative decalcified histological images in HA, TCP and HA/Ca/Mg scaffolds, obtained from longitudinal sections with implants at the defects of the radius. (A–D) H&E, Safranin O-fast green, Giemsa and Sirius red staining (×5, ×100) at weeks 4 and 8 after implantation. M: materials, NB: newly formed bone, F: fibrous tissue.

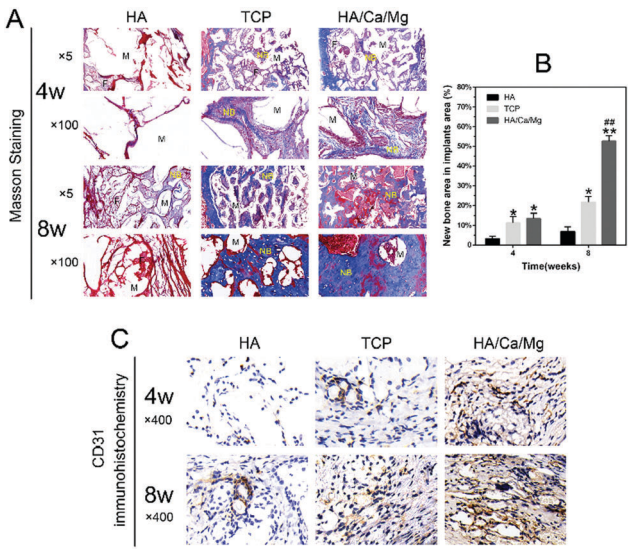

Fig. 5 Representative decalcified histological images used to evaluate newly formed bones in HA, TCP and HA/Ca/Mg scaffolds, obtaining from longitudinal sections with implants at the defects of the radius. (A) Masson's trichrome staining (×5, ×100) at weeks 4 and 8 after implantation. (B) Quantitative analysis of the new bone area in stained sections at weeks 4 and 8 after implantation. (C) CD31 immunohistochemistry (×400) used to assess vascularization at weeks 4 and 8 after implantation. M: materials, NB: newly formed bone, F: fibrous tissue. *$p < 0.05$ compared with HA scaffolds. **$p < 0.01$ compared with HA scaffolds. $^{\#\#}p < 0.01$ compared with TCP scaffolds.

covered with abundant bone tissues, especially in the central region of the scaffold. The quantitative results of newly formed bones in the osteointegration process are shown in Fig. 6B. At weeks 4 and 8, the HA/Ca/Mg group indicated the most compelling bone growth inside implants at the defects of the radius and displayed the best osteogenesis among all groups ($p < 0.05$ at week 4, and $p < 0.01$ at week 8). Moreover, the newly formed bones inside the implants were fluorescently labelled and observed by CLSM; the results are given in Fig. 6C. A greenish yellow fluorescence was observed due to calcein labelling, while a red fluorescence was observed according to alizarin red labelling. The fluorescence could be used to exquisitely investigate the osteogenic process. The images implied that the HA/Ca/Mg scaffold formed the largest region of the mature mineralized bone tissue at week 8. The quantitative results of fluorescence labelling were consistent with those of Van Gieson staining, which suggested that the HA/Ca/Mg scaffold had the best osteogenic capacity at both weeks 4 and 8 (Fig. 6D, $p < 0.05$ at week 4, $p < 0.01$ at week 8). It is well known that the surface characteristics of biomaterials, such as composition, topography, and ion release, are very important for osseointegration.[46,47] We believe that the improved osteointegration around the HA/Ca/Mg scaffold might be due to the synergistic effect of a combination of factors.

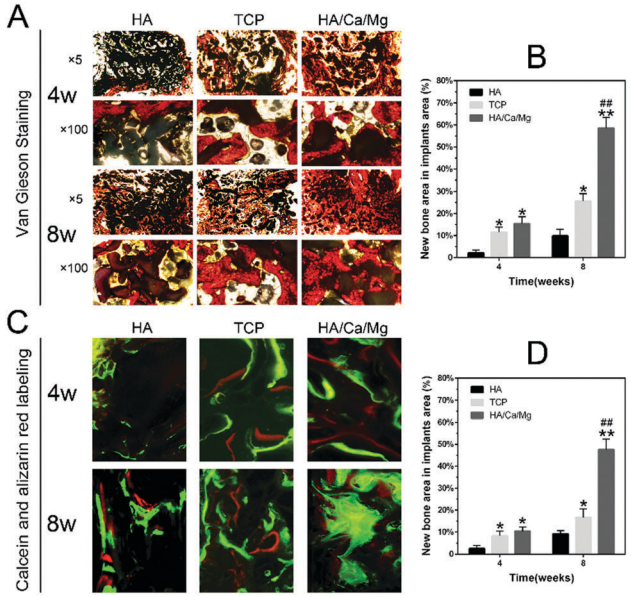

Fig. 6 Representative undecalcified histological images used to evaluate newly mineralized bones and osteointegration processes in HA, TCP and HA/Ca/Mg scaffolds, obtained from transverse sections with implants at the defects of the radius. (A) Van Gieson staining (×5, ×100) at weeks 4 and 8 after implantation. (B) Quantitative analysis of the new bone area in Van Gieson staining. (C) Fluorescence micrographs labelled by calcein and alizarin red at weeks 4 and 8 after implantation. Green, calcein. Red, alizarin red. (D) Quantitative analysis of the new bone area in fluorescence labelling. $^{*}p < 0.05$ compared with HA scaffolds. $^{**}p < 0.01$ compared with HA scaffolds. $^{\#\#}p < 0.01$ compared with TCP scaffolds.

4. Conclusion

In this research we have demonstrated the excellent capacity of our previously developed bioactive macroporous scaffold with interconnected porous structures and nano-crystal surface microstructures capable of releasing bioactive ions for bone regeneration. A variety of techniques were used to systematically investigate the bond regeneration efficacy *in vivo*. Due to synergistic effects on the bone healing process, the bioactive scaffold exhibited outstanding osteogenesis, vascularization and osseointegration, as evidenced in a rabbit radial segmental bone defect model. In summary, the scaffold developed during this research might be considered as a good clinical candidate as a bone substitute or tissue engineering scaffold.

Conflicts of interest

There are no conflicts of interest to declare.

Acknowledgements

This research was financially supported by the National Key R&D Program (2016YFC1102100), the China Postdoctoral Science Foundation (2018M630407), the Ningbo Municipal Natural Science Foundation (2010C500009) and the Zhejiang Natural Science Foundation (2017LY17H060001). X.-P. He thanks the Natural Science Foundation of China (21722801 and 21572058) and the Shanghai Rising-Star Program (16QA1401400) (to X.-P. He) for generous financial support. The Catalysis And Sensing for our Environment (CASE) network is thanked for research exchange opportunities. T. D. J. wishes to thank the Royal Society for a Wolfson Research Merit Award and ECUST for a guest professorship.

References

1 X. Zhang, H. A. Awad, R. J. O'Keefe, R. E. Guldberg and E. M. Schwarz, *Clin. Orthop. Relat. Res.*, 2008, **466**, 1777–1787.
2 V. M. Goldberg and S. Stevenson, *Clin. Orthop. Relat. Res.*, 1987, **225**, 7–16.
3 K. Jahan and M. Tabrizian, *Biomater. Sci.*, 2016, **4**, 25–39.
4 T. Tang and L. Qin, *J. Orthop. Translat.*, 2016, **5**, 69–71.
5 Z. Hao, Z. Song, J. Huang, K. Huang, A. Panetta, Z. Gu and J. Wu, *Biomater. Sci.*, 2017, **5**, 1382–1392.
6 E. S. Place, N. D. Evans and M. M. Stevens, *Nat. Mater.*, 2009, **8**, 457–470.
7 H. Lu, T. Hoshiba, N. Kawazoe and G. Chen, *Biomaterials*, 2011, **32**, 2489–2499.
8 X. Liu, C. Bao, H. H. Xu, J. Pan, J. Hu, P. Wang and E. Luo, *Acta Biomater.*, 2016, **42**, 378–388.
9 J. Brandt, S. Henning, G. Michler, W. Hein, A. Bernstein and M. Schulz, *J. Mater. Sci.: Mater. Med.*, 2010, **21**, 283–294.
10 E. Culverwell, S. C. Wimbush and S. R. Hall, *Chem. Commun.*, 2008, 1055–1057.
11 X. Li, Y. Zhao, Y. Bing, Y. Li, N. Gan, Z. Guo, Z. Peng and Y. Zhu, *ACS Appl. Mater. Interfaces*, 2013, **5**, 5557–5562.
12 T. Miyazaki, C. Matsunami and Y. Shirosaki, *Mater. Sci. Eng., C*, 2017, **70**, 71–75.
13 Z. Ozdemir, A. Ozdemir and G. B. Basim, *Mater. Sci. Eng., C*, 2016, **68**, 383–396.
14 L. Chu, G. Jiang, X. L. Hu, T. D. James, X. P. He, Y. Li and T. Tang, *J. Mater. Chem. B*, 2018, **6**, 1658–1667.
15 J. Wu, K. Zhang, X. Yu, J. Ding, L. Cui and J. Yin, *Biomater. Sci.*, 2017, **5**, 2251–2267.
16 L. Zheng, F. Yang, H. Shen, X. Hu, C. Mochizuki, M. Sato, S. Wang and Y. Zhang, *Biomaterials*, 2011, **32**, 7053–7059.
17 I. Bajpai, D. Y. Kim, J. Kyong-Jin, I. H. Song and S. Kim, *J. Biomed. Mater. Res., Part B*, 2017, **105**, 72–80.
18 S. H. Chen, M. Lei, X. H. Xie, L. Z. Zheng, D. Yao, X. L. Wang, W. Li, Z. Zhao, A. Kong, D. M. Xiao, D. P. Wang, X. H. Pan, Y. X. Wang and L. Qin, *Acta Biomater.*, 2013, **9**, 6711–6722.
19 C. Li, C. Jiang, Y. Deng, T. Li, N. Li, M. Peng and J. Wang, *Sci. Rep.*, 2017, **7**, 41331.
20 J. O. Hollinger and J. C. Kleinschmidt, *J. Craniofac. Surg.*, 1990, **1**, 60–68.
21 S. D. Cook, M. W. Wolfe, S. L. Salkeld and D. C. Rueger, *J. Bone Jt. Surg., Am. Vol.*, 1995, **77**, 734–750.
22 C. Wan, Q. He and G. Li, *J. Orthop. Res.*, 2006, **24**, 610–618.
23 Y. X. He, G. Zhang, X. H. Pan, Z. Liu, L. Z. Zheng, C. W. Chan, K. M. Lee, Y. P. Cao, G. Li, L. Wei, L. K. Hung, K. S. Leung and L. Qin, *Bone*, 2011, **48**, 1388–1400.

24 Y. Yang, S. Yang, Y. Wang, Z. Yu, H. Ao, H. Zhang, L. Qin, O. Guillaume, D. Eglin, R. G. Richards and T. Tang, *Acta Biomater.*, 2016, **46**, 112–128.
25 G. Liu, J. Sun, Y. Li, H. Zhou, L. Cui, W. Liu and Y. Cao, *Calcif. Tissue Int.*, 2008, **83**, 176–185.
26 I. C. Tuncay, B. H. Ozdemir, H. Demirors, O. Karaeminogullari and N. R. Tandogan, *J. Invest. Surg.*, 2005, **18**, 115–122.
27 W. Lu, K. Ji, J. Kirkham, Y. Yan, A. R. Boccaccini, M. Kellett, Y. Jin and X. B. Yang, *Cell Tissue Res.*, 2014, **356**, 97–107.
28 R. Ma, Z. Yu, S. Tang, Y. Pan, J. Wei and T. Tang, *Int. J. Nanomed.*, 2016, **11**, 6023–6033.
29 Y. Liu, J. K. Chan and S. H. Teoh, *J. Tissue Eng. Regener. Med.*, 2015, **9**, 85–105.
30 I. Zderic, P. Steinmetz, L. M. Benneker, C. Sprecher, O. Röhrle, M. Windolf, A. Boger and B. Gueorguiev, *J. Orthop. Translat.*, 2017, **8**, 40–48.
31 J. H. Lee, H. L. Jang, K. M. Lee, H. R. Baek, K. Jin, K. S. Hong, J. H. Noh and H. K. Lee, *Acta Biomater.*, 2013, **9**, 6177–6187.
32 Y. Wen, S. Xun, M. Haoye, S. Baichuan, C. Peng, L. Xuejian, Z. Kaihong, Y. Xuan, P. Jiang and L. Shibi, *Biomater. Sci.*, 2017, **5**, 1690–1698.
33 S. Kargozar, N. Lotfibakhshaiesh, J. Ai, M. Mozafari, P. Brouki-Milan, S. Hamzehlou, M. Barati, F. Baino, R. G. Hill and M. T. Joghataei, *Acta Biomater.*, 2017, **58**, 502–514.
34 S. Ali, A. Singh, A. A. Mahdi and R. N. Srivastava, *J. Orthop. Translat.*, 2017, **10**, 5–11.
35 M. Oates, R. Chen, M. Duncan and J. A. Hunt, *Biomaterials*, 2007, **28**, 3679–3686.
36 J. Barralet, U. Gbureck, P. Habibovic, E. Vorndran, C. Gerard and C. J. Doillon, *Tissue Eng., Part A*, 2009, **15**, 1601–1609.
37 W. Katagiri, T. Kawai, M. Osugi, Y. Sugimura-Wakayama, K. Sakaguchi, T. Kojima and T. Kobayashi, *Plast. Reconstr. Surg.*, 2017, **39**, 1–8.
38 E. Schipani, C. Maes, G. Carmeliet and G. L. Semenza, *J. Bone Miner. Res.*, 2009, **24**, 1347–1353.
39 V. Karageorgiou and D. Kaplan, *Biomaterials*, 2005, **26**, 5474–5491.
40 S. Fahmy-Garcia, M. van Driel, J. Witte-Buoma, H. Walles, J. P. van Leeuwen, G. van Osch and E. Farrell, *Tissue Eng., Part A*, 2018, **24**, 207–218.
41 W. C. Liu, S. Chen, L. Zheng and L. Qin, *Adv. Healthcare Mater.*, 2017, **6**, 201600434.
42 T. M. Valverde, E. G. Castro, M. H. Cardoso, P. A. Martins-Junior, L. M. Souza, P. P. Silva, L. O. Ladeira and G. T. Kitten, *Life Sci.*, 2016, **162**, 115–124.
43 J.-S. Wang, M. Tägil, H. Isaksson, M. Boström and L. Lidgren, *J. Orthop. Translat.*, 2016, **6**, 10–17.
44 H. M. Kim, H. Takadama, T. Kokubo, S. Nishiguchi and T. Nakamura, *Biomaterials*, 2000, **21**, 353–358.
45 P. G. Coelho and R. Jimbo, *Arch. Biochem. Biophys.*, 2014, **561**, 99–108.
46 B. D. Boyan, T. W. Hummert, D. D. Dean and Z. Schwartz, *Biomaterials*, 1996, **17**, 137–146.
47 J. T. Steigenga, K. F. Al-Shammari, F. H. Nociti, C. E. Misch and H. L. Wang, *Implant Dent.*, 2003, **12**, 306–317.